Supplementary Information (SI) for Journal of Materials Chemistry A.
This journal is © The Royal Society of Chemistry 2026

Electronic supplementary information

Interface Strain Engineering of Ru-RuO$_x$/Graphene Aerogel Composite Boost HER, OER and ORR Applications

Hu Yao[a,‡], Bowen Song[b,c,‡], Xin Yu[a], Qiuhan Cao[a], Lei Li[a], Yucheng Huang[b,c,*], Xiaohui Guo[a,*]

[a] *Key Lab of Synthetic and Natural Functional Molecule Chemistry of Ministry of Education, The College of Chemistry and Materials Science, Northwest University, Xi'an 710069, P. R. China.*

[b] *College of Chemistry and Material Science, Key Laboratory of Functional Molecular Solids, Ministry of Education, Anhui Normal University, Wuhu 241000, China.*

[c] *Anhui Key Laboratory of Molecule-Based Materials, Anhui Carbon Neutrality Engineering Center, Anhui Normal University, Wuhu 241000, China.*

‡*Hu Yao and Bowen Song contributed to this work equally.*

*Corresponding authors: Yucheng Huang (huangyc@mail.ahnu.edu.cn); Xiaohui Guo (guoxh2009@nwu.edu.cn)

1. Experimental Section

1.1 Electrochemical measurements

The electrochemical measurements (HER and OER) performance were evaluated using a three-electrode system on the CHI 760E electrochemical station. The Hg/HgO (1 M KOH) was used as the reference electrode, while the counter and the working electrodes were Pt foil and the self-supported electrode, respectively. All the measured potentials vs Hg/HgO were converted to the reversible hydrogen electrode (RHE). In 1 M KOH, $E_{\mathrm{RHE}}= E_{\mathrm{Hg/HgO}}+0.0977\ \mathrm{V}+0.059*\mathrm{pH}$. The working electrodes were first activated using the cyclic voltammetry (CV) test at a scan rate of 50 mV s^{-1} several times, and then linear sweep voltammetry (LSV) tests were conducted. The Tafel slope was obtained from the LSV curves. To test the electrochemical stability of Ru/GA and other samples in 1 M KOH, a long-term chronopotentiometry was performed at the current density of 10 or 100 mA cm^{-2}. The electrochemically active surface area (ECSA) was determined by measuring the CV scan rate dependence with respect to the capacitive current associated with the double-layer charging. The ECSA was evaluated by the following equation:

$$\mathrm{ECSA} = C_{dl}/0.04\ \mathrm{mF\ cm^{-2}}$$

The ORR was conducted under basic conditions (0.1 M KOH). Differences from the HER and OER tests are the reference electrode is Ag/AgCl, $E_{\mathrm{RHE}}=E_{\mathrm{Ag/AgCl}}+0.197\ \mathrm{V}+0.059*\mathrm{pH}$. For comparison, commercial Pt/C and other samples were used as the contrast catalysts.

1.2 Overall Water Splitting measurements

A two-electrode cell was fabricated to conduct the assisted OER/HER electrocatalysis Overall Water Splitting test (1 M KOH). The cathode and anode materials were both the Ru-RuO_x/GA-2 electrode. For comparison, commercial RuO_2 and 20%Pt/C were used as the OER/HER electrocatalysis Overall Water Splitting test (1 M KOH). The cathode and anode materials were first activated using the CV test at a scan rate of 50 mV s^{-1} several times, and then linear sweep voltammetry (LSV) tests were conducted. To test the electrochemical stability of Overall Water Splitting in 6 M KOH, a long-term chronopotentiometry was performed at 500 mA cm^{-2}. The O_2/H_2 produced by the cathode was collected by the drainage and gas-collecting method for quantitative analysis.

1.3 Zinc–air battery tests

The prepared air electrode and a polished Zn plate (thickness 5 mm) were assembled in 6.0 M KOH and

0.2 M $Zn(CH_3COO)_2$ electrolyte. For air electrode preparation: 4 mg catalyst powders were dispersed into an ethanol solution containing 760 μL ethanol and 40 μL Nafion solution (5 wt%) under sonication for 1 h. Then the obtained homogeneous catalyst inks were uniformly dropcast onto carbon paper (2×2 cm^2) to reach a loading of 1 mg cm^{-2} and the effective area (S) exposed to the electrolyte was 1 cm^2, and a Ni mesh was used as the current collector. For the assembly of the battery for comparison, a commercial catalyst (20 wt % Pt/C: RuO_2 = 1:1, mass ratio) was used with the same loading amount. For the Zn-air batteries test: the discharge/charge tests were conducted on a CHI 760E electrochemical working station at a scan rate of 5 mV s^{-1}. The galvanostatic discharge-charge curves were recorded using a LAND testing system at a current density of 10 mA cm^{-2} with 10 min per cycle (charge 5 min and discharge 5 min). The specific capacity and energy density were calculated from the galvanostatical discharge results, normalized to the mass of consumed Zn. The mass of consumed Zn was determined by the mass difference between the fresh Zn and resultant anode after discharging. The energy density, specfic capacity and power density of primary Zn-air battery were calculated based on the applied current (I), average discharge voltage (V), service hours (t), the weight of zinc consumed (m_{Zn}) and the effective area (S) exposed to the electrolyte for the air electrode.

$$\text{Specfic capacity } (\mathrm{mAh\,g^{-1}}) = \frac{I\times t}{m_{Zn}}$$

$$\text{Power density } (\mathrm{mW\,cm^{-2}}) = \frac{I\times V}{S}$$

1.4 The density functional theory calculations

All the spin-polarized DFT calculations were performed using the projector augmented wave method (PAW)[1] as implemented in the Vienna Ab initio Simulation Package (VASP) [2]. The generalized gradient approximation (GGA) with the Perdew-Burke-Ernzerhof functional (PBE)[3] was used to describe the exchange-correlation interactions, and the van der Waals (vdW) correction proposed by Grimme (DFT-D3)[4] was included in describing the long-range interactions. The cutoff energy of the plane-wave was set to 500 eV. Ab initio molecular dynamics (AIMD) simulations in constant temperature and volume with a Nose–Hoover thermostat[5] were adopted to evaluate the thermodynamic stability of the materials. All the structures were relaxed until the residual atomic forces on each atom were less than 0.02 eV/Å, and the total energy was less than 10^{-6} eV for self-consistent field (SCF) calculations. To improve the accuracy and efficiency, the Brillouin zone integration was performed on the 3 × 3 × 1 Monkhorst–Pack k-point mesh.[6] The vacuum space was set to 15 Å in the z-direction to avoid interactions between periodic images.

The $4e^-$ OER mechanism in acidic media is listed as follows:

$$* + H_2O(l) \rightarrow {*OH} + H^+ + e^- \quad (1)$$

$$*OH \rightarrow {*O} + H^+ + e^- \quad (2)$$

$$*O + H_2O(l) \rightarrow {*OOH} + H^+ + e^- \quad (3)$$

$$*OOH \rightarrow O_2(g) + * + H^+ + e^- \qquad (4)$$

The adsorption energies of three reaction intermediates (*OH, *O, and *OOH) in OER are calculated as follows:

$$\Delta E_{DFT}(*OH) = E_{DFT}(*OH) - E(*) - [E_{DFT}(H_2O) - 1/2*E_{DFT}(H_2)] \qquad (5)$$

$$\Delta E_{DFT}(*O) = E_{DFT}(*O) - E(*) - [E_{DFT}(H_2O) - E_{DFT}(H_2)] \qquad (6)$$

$$\Delta E_{DFT}(*OOH) = E_{DFT}(*OOH) - E(*) - [2* E_{DFT}(H_2O) - 3/2* E_{DFT}(H_2)] \qquad (7)$$

where the $E_{DFT}(*OH)$, $E_{DFT}(*O)$, $E(*)$, $E_{DFT}(H_2O)$, and $E_{DFT}(H_2)$ indicate the total energy of *OH, *O, substrate, H_2O molecular, H_2 molecular, separately. The free energies of O_2, H_2O, and H_2 are listed in Table 1.

The free energy change (ΔG) of each elementary step is calculated as , where is the zero-point energy change, is the enthalpy-temperature correction, and is the entropy change, respectively. Gibbs adsorption free energy corrections (ΔGcorr = $\Delta ZPE + \int C_P dT - T\Delta S$) for each intermediate during OER are listed in Table 2.

Table 1. The DFT energies (E_{DFT}) and corresponding free energy correction values (ΔG) of $H_2(g)$ and $H_2O(l)$ are calculated at 1 bar and 0.035 bar. Due to the fact that O_2 is poorly described in DFT calculations, the free energy of O_2 is calculated by $GO_2 = 2GH_2O - 2GH_2 + 4.92$ eV. The DFT energies of H_2 and H_2O were calculated in a 10 Å × 10 Å × 10 Å unit cell in vacuum.

	Pressure(bar)	**Temperature(K)**	**E(DFT)(eV)**	**ΔG(eV)**	**G(eV)**
H_2O(l)	0.035	298.15	-14.22	0.00	-14.22
H_2(g)	1.00	298.15	-6.77	-0.044	-6.81
O_2(g)	1.00	298.15	/	/	-9.90

Table 2. Gibbs adsorption free energy corrections (ΔGcorr = $\Delta ZPE + \int C_P dT - T\Delta S$) for each intermediate during OER.

Species	***OH**	***O**	***OOH**
G_{corr}/eV	0.27	0.028	0.34

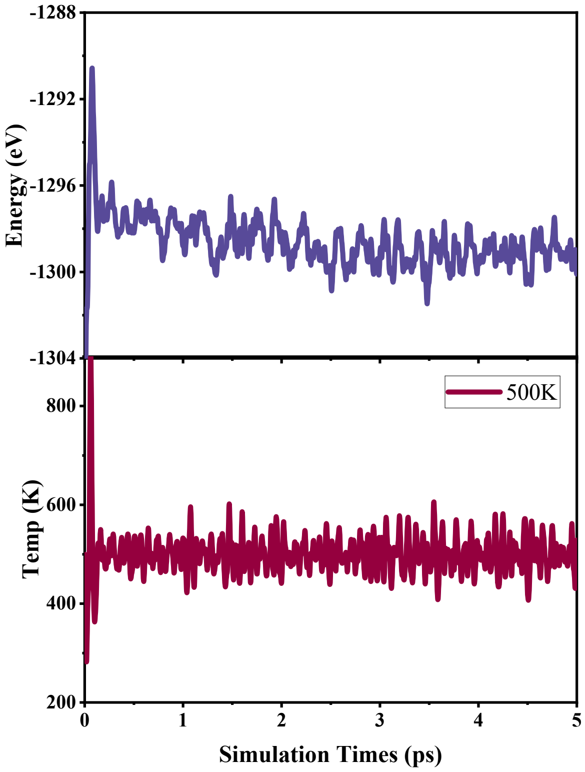

Figure S1. The atomic structure and system energy obtained by AIMD calculation for $RuO_x(110)$-Ru(101). The fluctuation of temperature concerning the duration for AIMD simulations of $RuO_x(110)$-Ru(101) under 500 K in 5 ps.

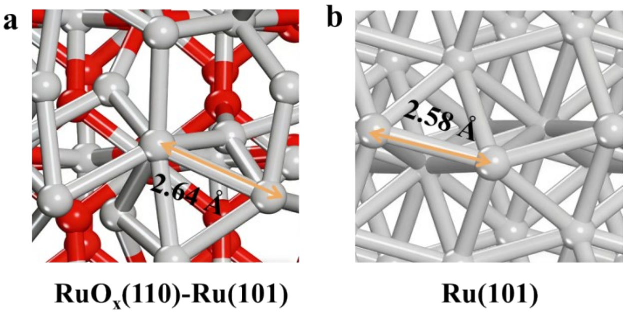

Figure S2. Simulative structural model of Ru−Ru bond in (a) $RuO_x(110)$-Ru(101) and (b) Ru(101) model.

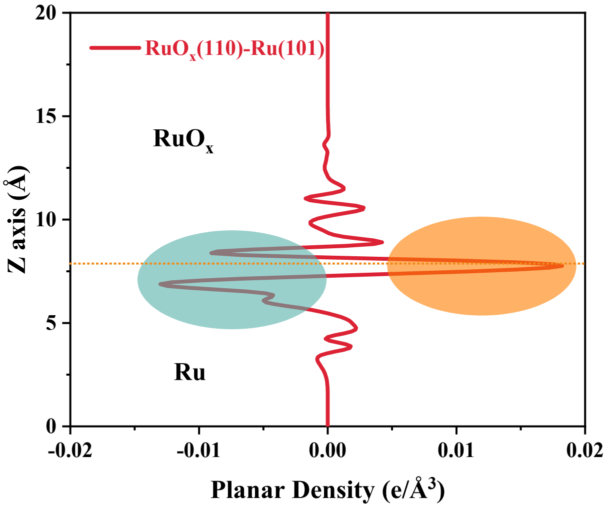

Figure S3. Planar-averaged electron density difference Δρ (Z) of RuO$_x$(110)-Ru(101).

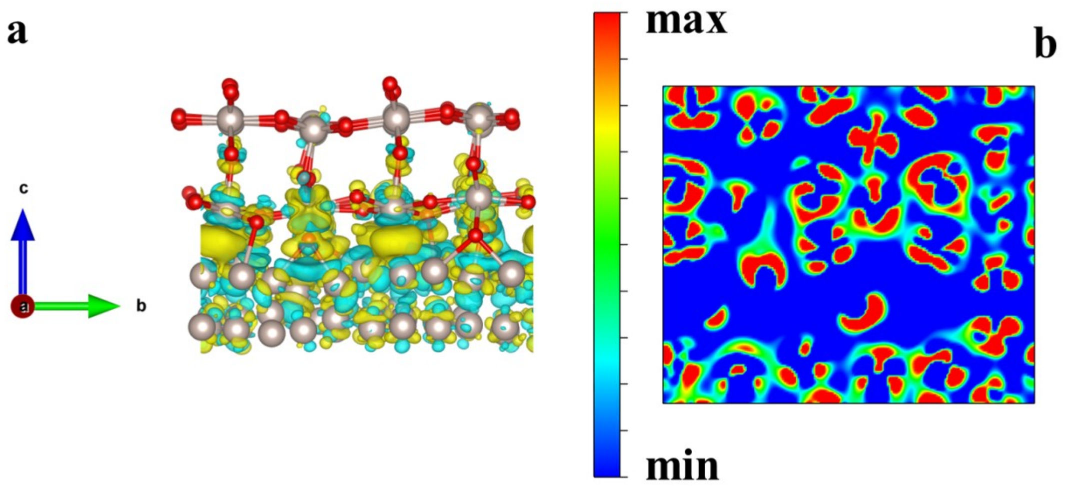

Figure S4. Differential charge density of RuO$_x$(110)-Ru(101). (a) Side-view. Yellow: electron accumulation, cyan: electron depletion. (b). Two-dimensional projection of the Ru site of RuO$_x$(110) with differential charge density at the interface.

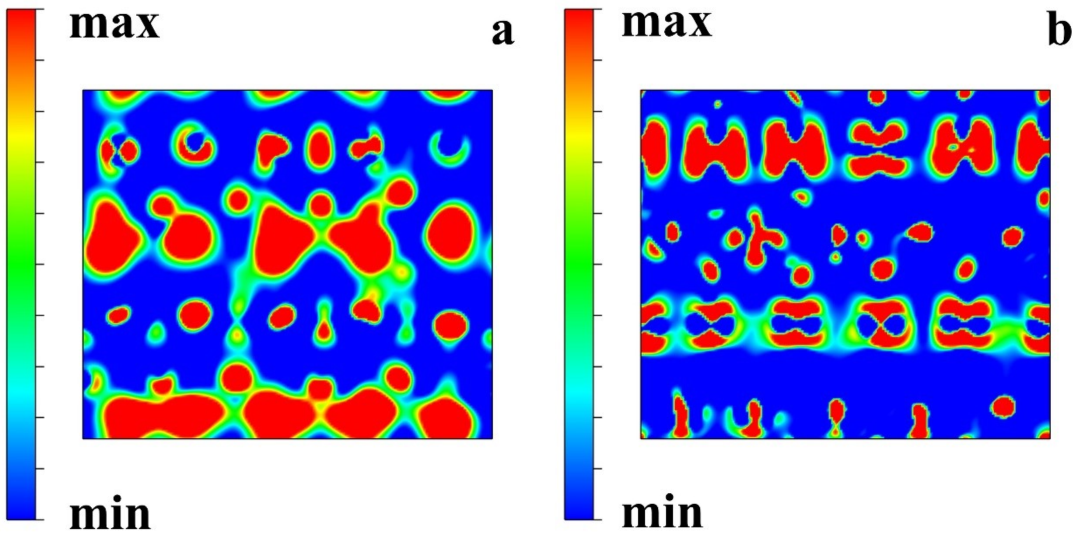

Figure S5. (a) Two-dimensional projection of the O site of RuO$_x$(110) with differential charge density at the interface. (b). Two-dimensional projection of the Ru site of Ru (101) with differential charge density at the interface.

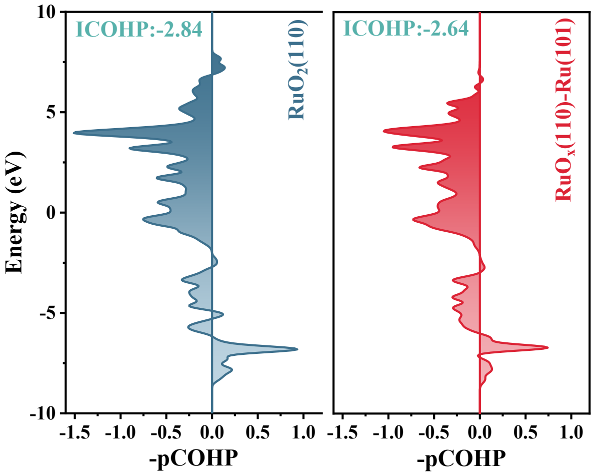

Figure S6. Calculated pCOHP diagrams for RuO_2(110) and RuO_x(110)-Ru(101).

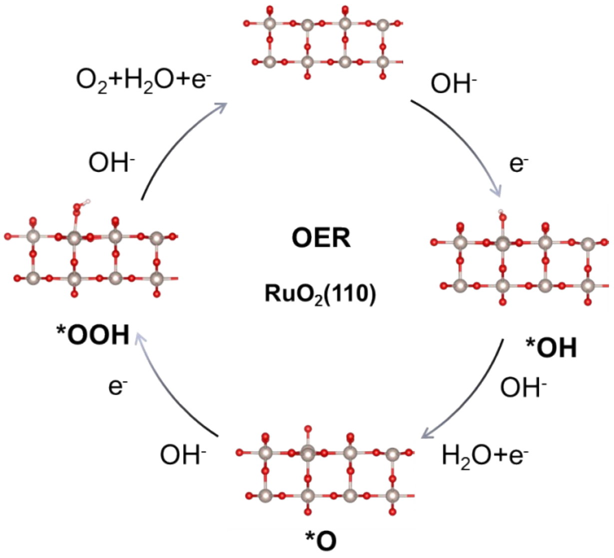

Figure S7. DFT optimized structures for OER reaction intermediates adsorbed on pristine RuO_2(110).

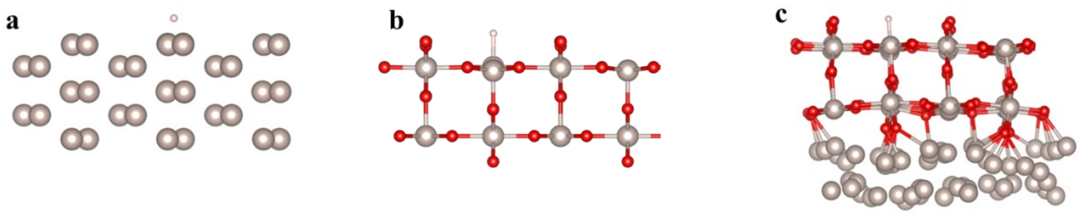

Figure S8. (a-c) The optimized structure of * H adsorbed on the Ru site of (a) Ru(101), (b) RuO_2(110), and (c) RuO_x(110)-Ru(101), respectively.

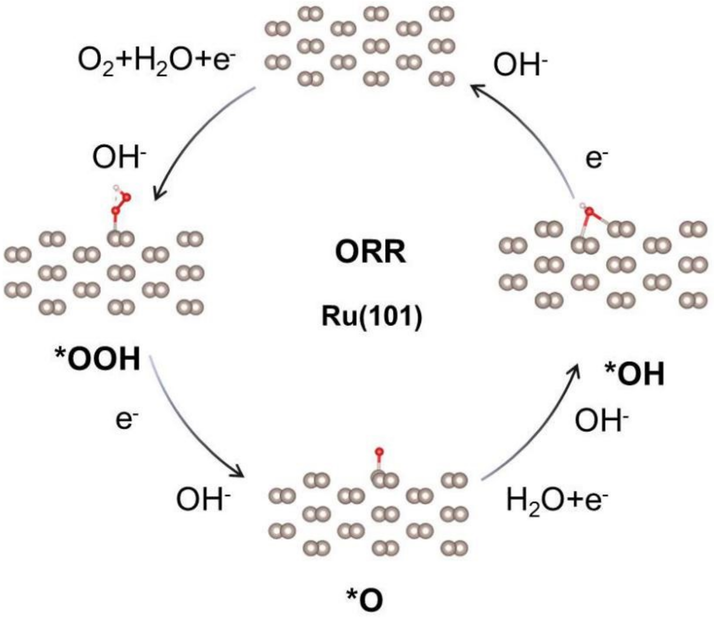

Figure S9. DFT optimized structures for ORR reaction intermediates adsorbed on pristine Ru(101).

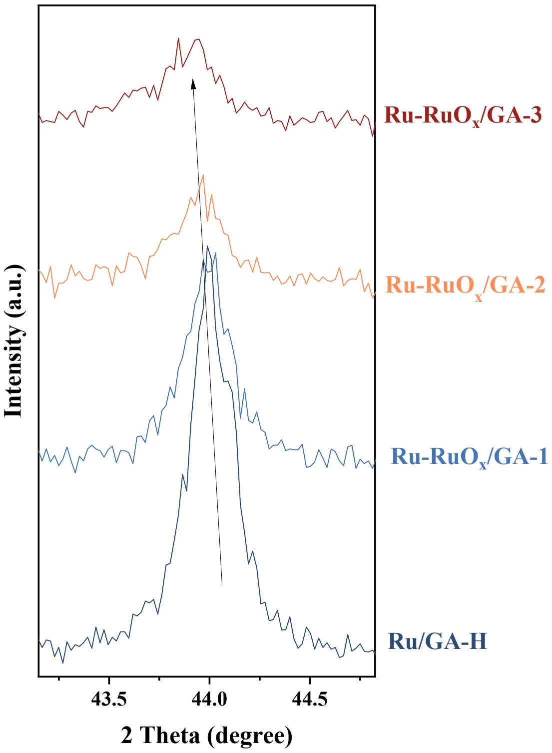

Figure S10. XRD localized magnification of Ru/GA-H and Ru-RuO$_x$/GA-1, 2, 3.

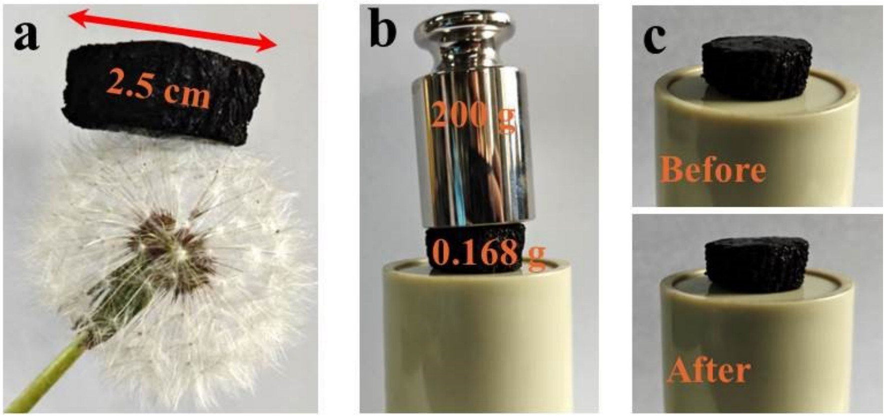

Figure S11. (a) optical image of GA. (b, c) optical photographs of GA before and after stress tests.

The porous GA precursor was obtained by using NaCl as template, and then the final sample was obtained by solution adsorption and two-step calcination processes [7]. Notably, the mass density of GA is extremely low, and the dandelion can easily bear the weight of a piece of carbon aerogel (~6 cm^3) without deformation of the dandelion (Fig. S11a). Moreover, the GA has excellent compressive properties and can withstand a weight of 1200 times its own weight without deformation (Fig. S11b, c). This suggests that the GA obtained by this method has a rich porous structure, which serves as a substrate material that helps to reduce the agglomeration of the catalyst [8].

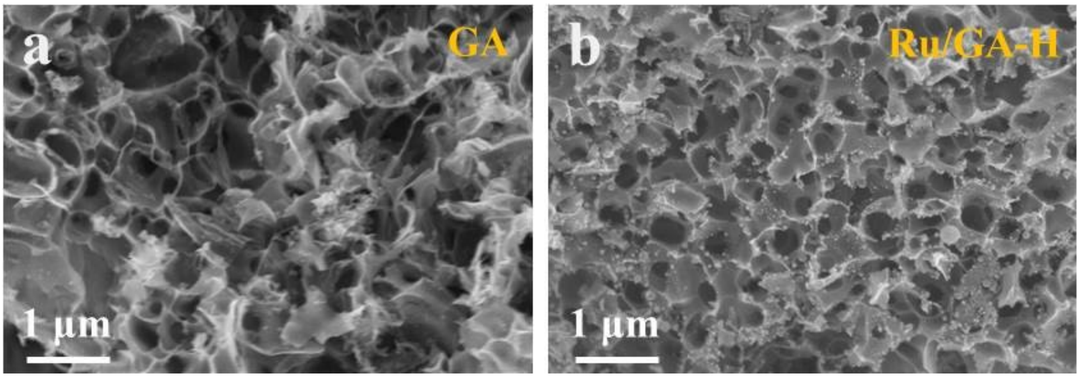

Figure S12. SEM images of (a) GA and (b) Ru/GA-H.

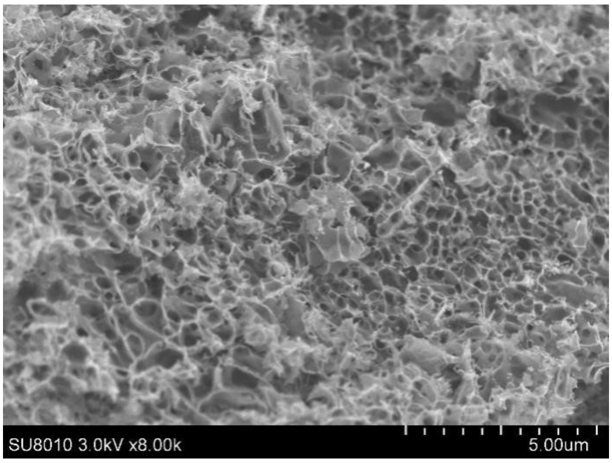

Figure S13. SEM image of Ru/GA-H.

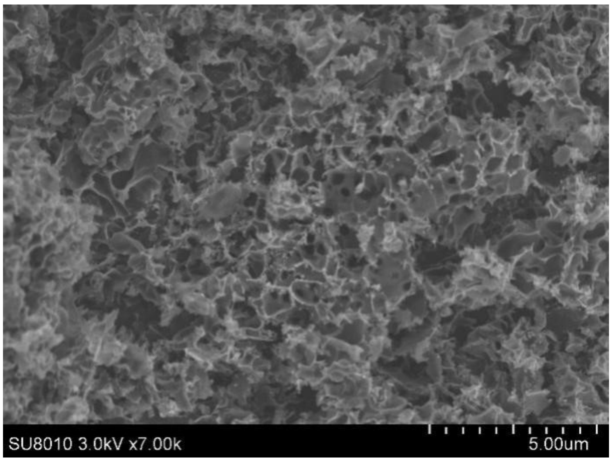

Figure S14. SEM image of Ru-RuO$_x$/GA-1.

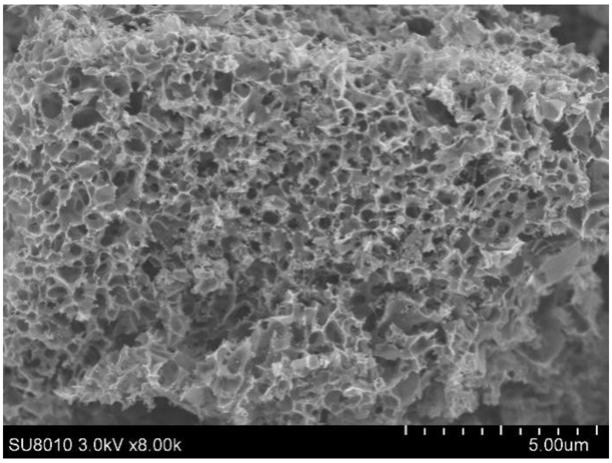

Figure S15. SEM image of Ru-RuO$_x$/GA-2.

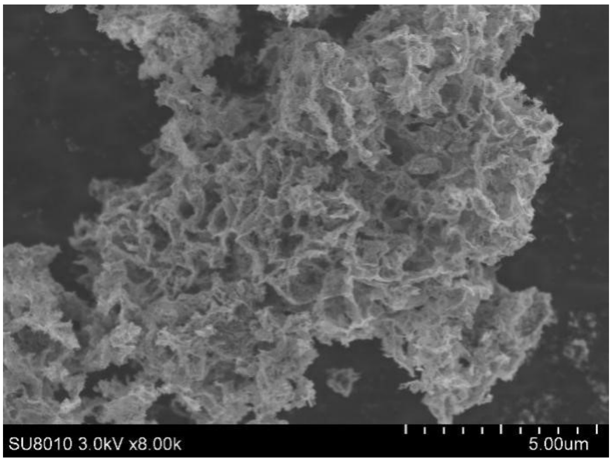

Figure S16. SEM image of Ru-RuO$_x$/GA-3.

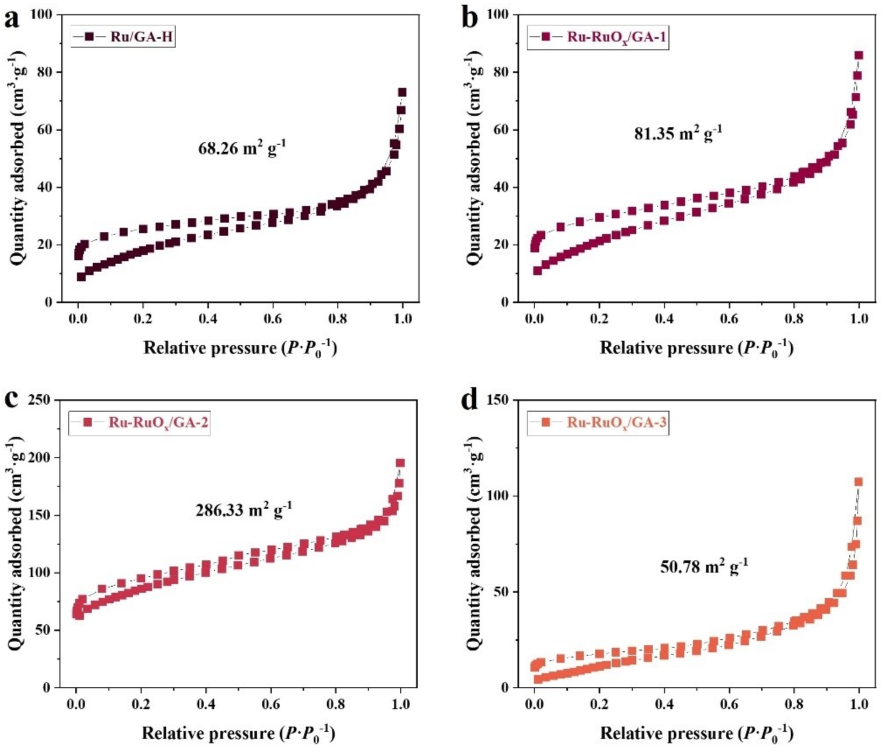

Figure S17. (a) N_2 sorption isotherms of Ru/GA-H and Ru-RuO_x/GA-1, 2, 3.

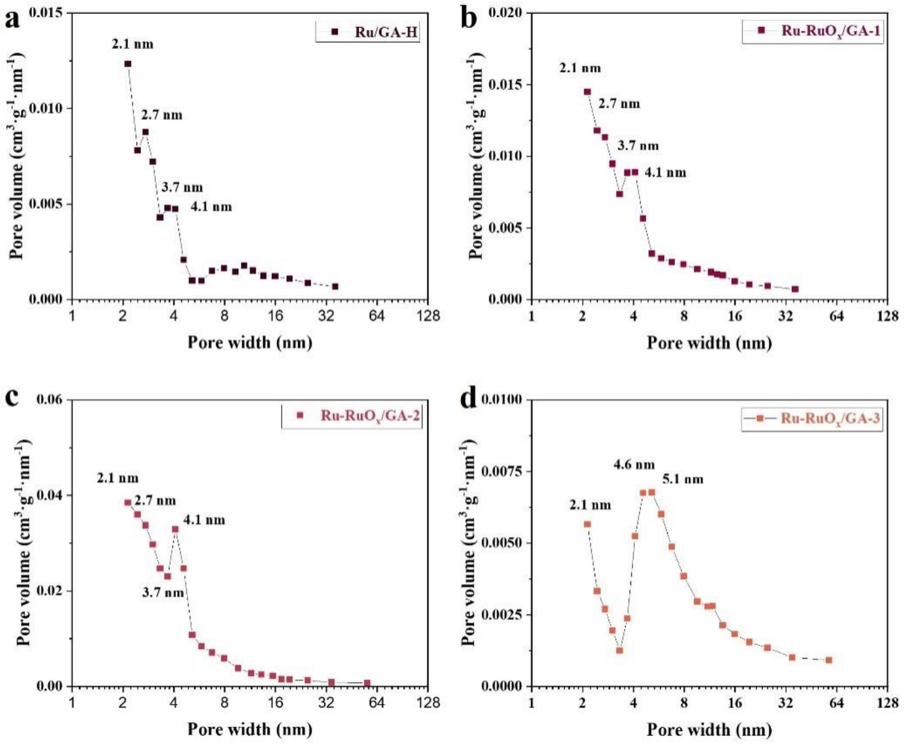

Figure S18. (a) The corresponding pore size distribution of Ru/GA-H and Ru-RuO_x/GA-1. 2. 3.

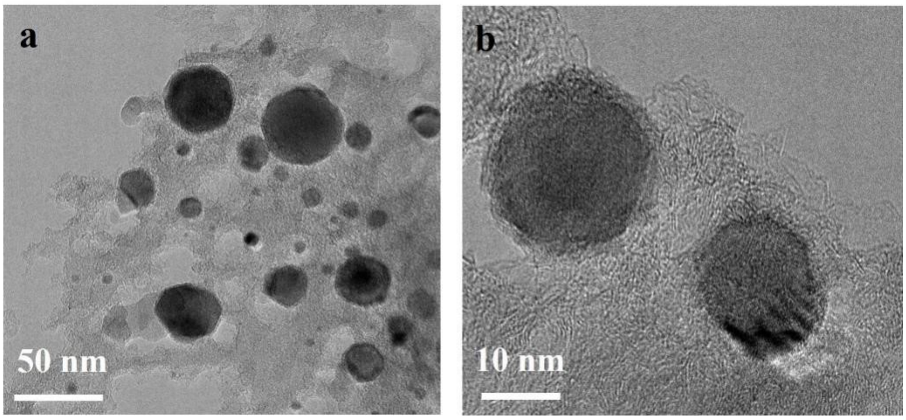

Figure S19. TEM images of Ru/GA-H.

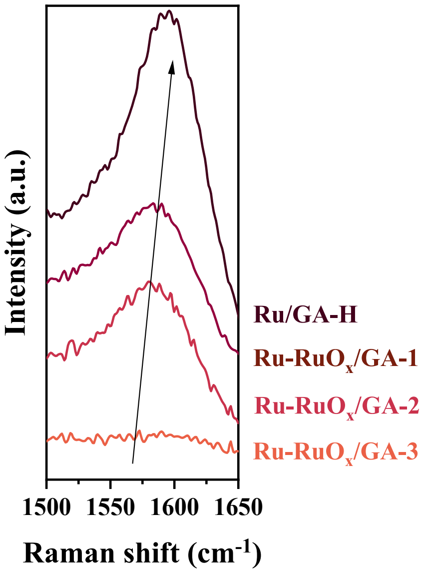

Figure S20. local magnification Raman spectra of Ru/GA-H, Ru-RuO$_x$/GA-1, 2, 3.

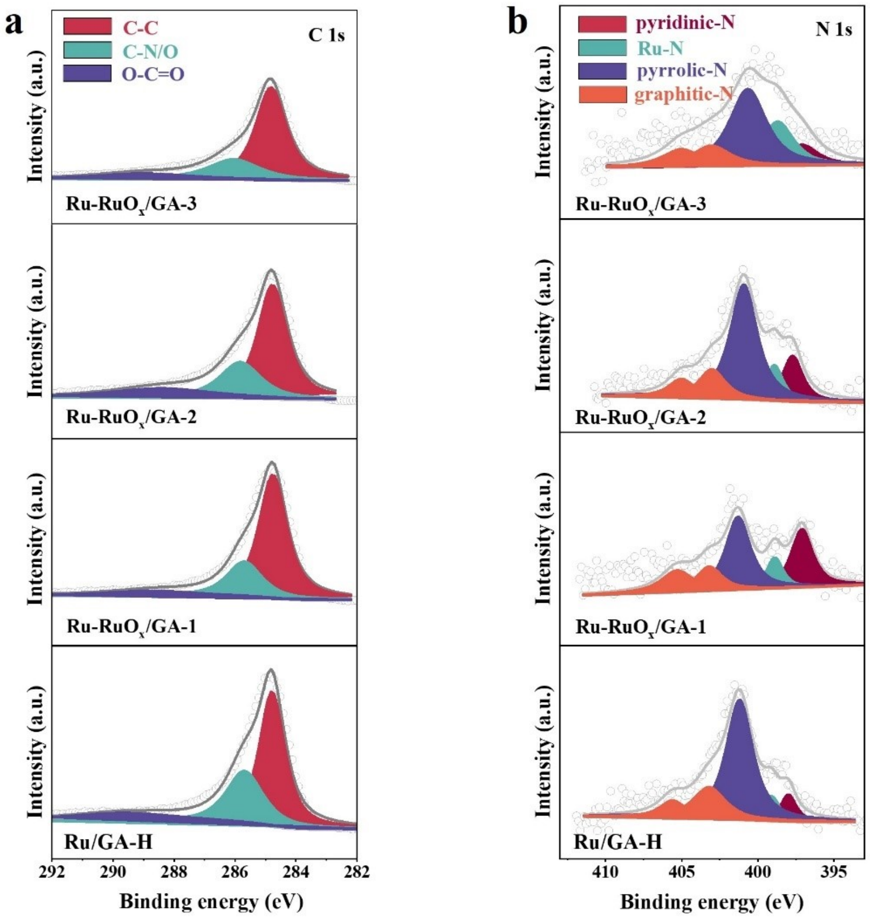

Figure S21. (a) C 1s and (b) N 1s XPS spectra of Ru/GA-H, Ru-RuO$_x$/GA-1, 2, 3.

In addition, the C 1s and N 1s XPS results of the catalysts were systematically analyzed as an indication of the bonding structure and changes in the substrate GA. As shown in Fig. S21a, the C 1s XPS results indicate the existence of three types of chemical bonds, C-C, C-N/O, and O-C=O, for GA [9]. Notably, the strength of these three types of chemical bonds weakened at the oxidation temperature of 450 °C, which indicated that the GA structure was damaged; the N 1s XPS results showed a similar situation, except that the Ru-N chemical bonds could be observed [9-11], and the spectral peaks of the N 1s spectrum of the 450 °C oxidation-treated Ru-RuO$_x$/GA-3 were weakened. This indicated that the oxidation temperature was on the high side, which was in agreement with the SEM, Raman, and BET test results, the preferred 350 °C is the suitable oxidation temperature (Fig. S21b).

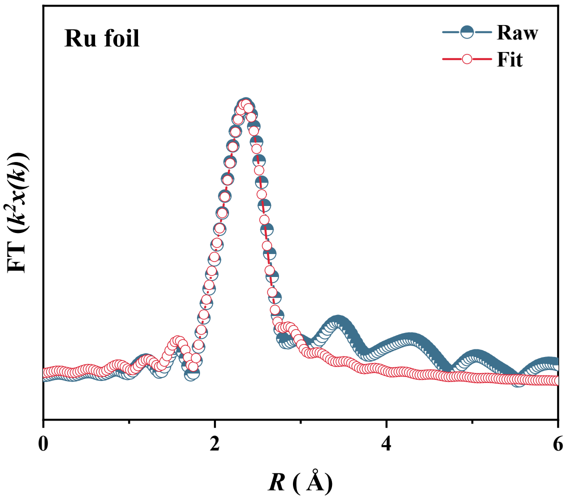

Figure S22. Ru K-edge EXAFS fitting curves of Ru foil in R space.

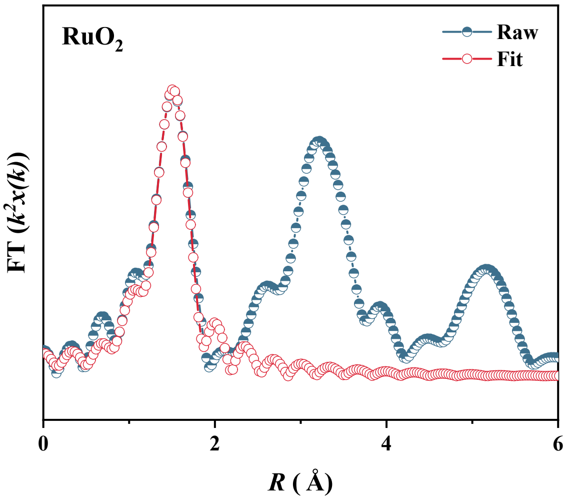

Figure S23. Ru K-edge EXAFS fitting curves of RuO_2 in R space.

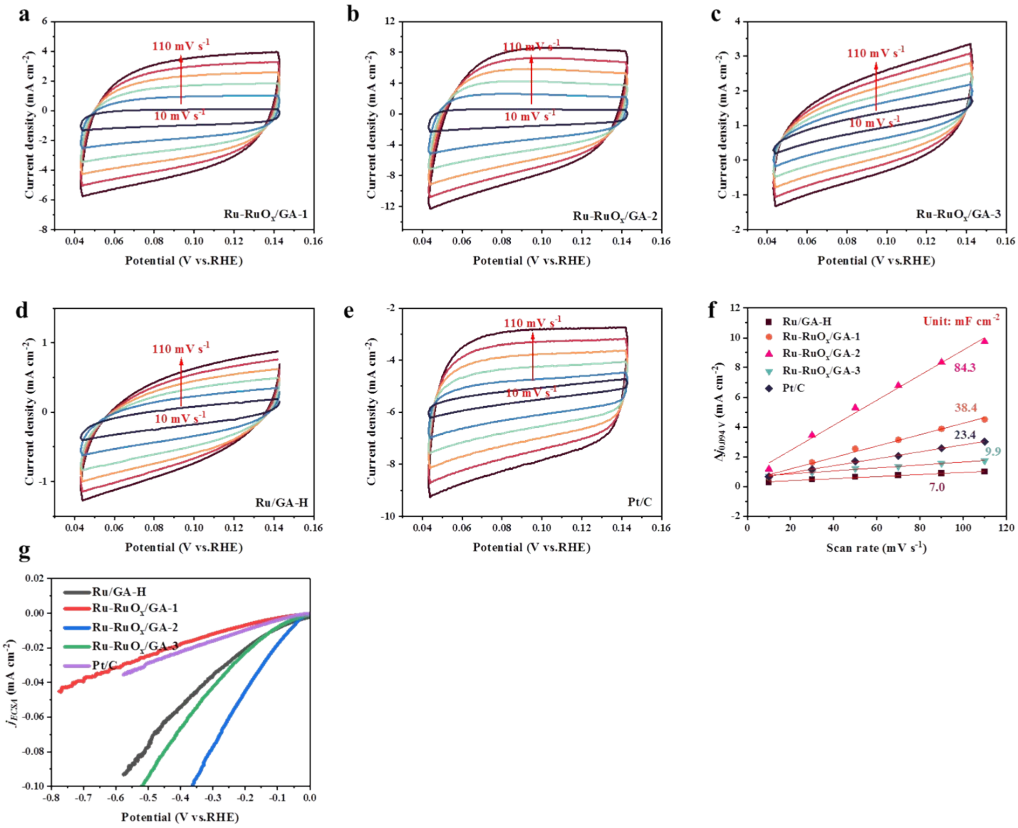

Figure S24. (a-e) CVs with different scan rates for Ru-RuO$_x$/GA-1, 2, 3, Ru/GA-H, and Pt/C. (f) C_{dl} values fitted according to CV curves. (g) Current densities (j_{ECSA}) normalized by ECSAs for HER.

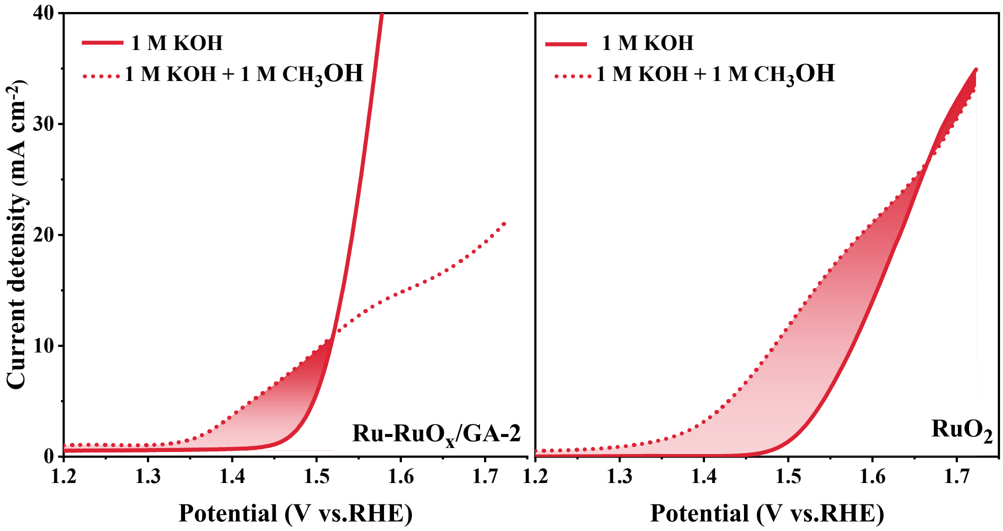

Figure S25. LSV curves for Ru-RuO$_x$/GA-2 and RuO$_2$ in 1 M KOH solution with (dashed lines) and without (solid lines) 1 M methanol.

Additionally, methanol was used as a probe to experimentally verify the weakened *OH adsorption. The methanol oxidation reaction (MOR) follows a well-established mechanism, where the nucleophilic reagent methanol readily adsorbs onto the electrophilic reagent *OH [12, 13]. Therefore, MOR is more active on surfaces with stronger *OH adsorption. When 1.0 M methanol was introduced into a 1 M KOH solution, the current density of Ru-RuO_x/GA-2 and RuO_2 showed a significant increase compared to before adding methanol, which is attributed to the electrooxidation of methanol. The current density difference caused by MOR was quantified by calculating the filled area between the curves, which is proportional to the number of transferred charges. The current difference observed between MOR and OER on Ru-RuO_x/GA-2 is smaller than that on RuO_2, indicating weaker MOR competitive reactions, which validates the weakened *OH on Ru-RuO_x/GA-2.

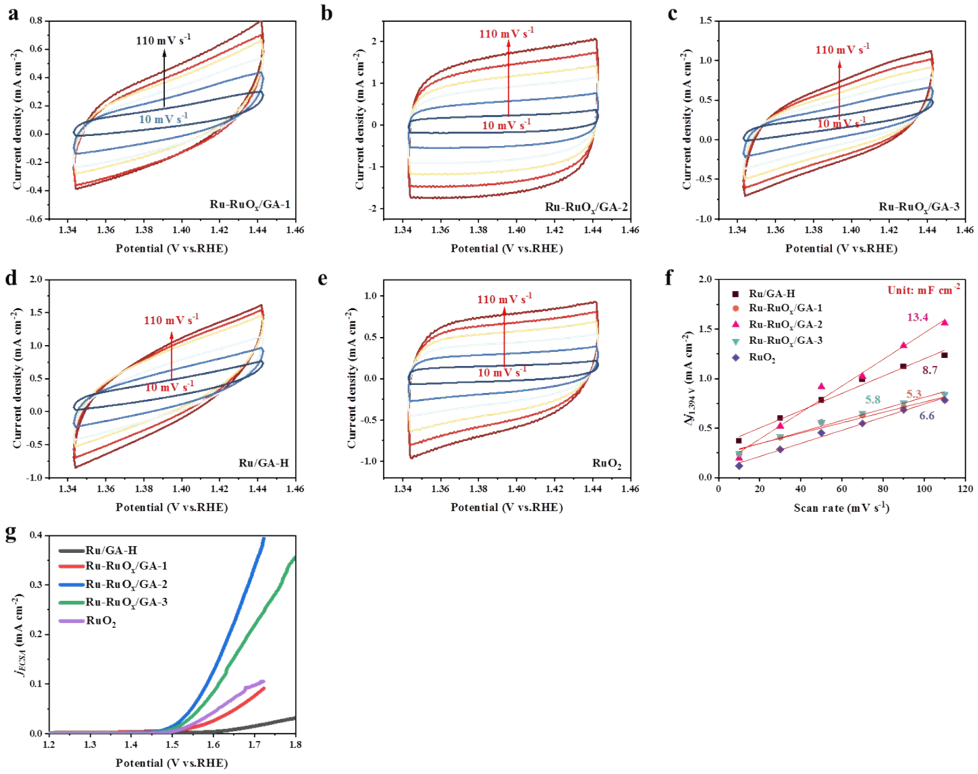

Figure S26. (a-e) CVs with different scan rates for Ru-RuO_x/GA-1, 2, 3, Ru/GA-H, and Pt/C. (f) C_{dl} values fitted according to CV curves. (g) Current densities (j_{ECSA}) normalized by ECSAs for OER.

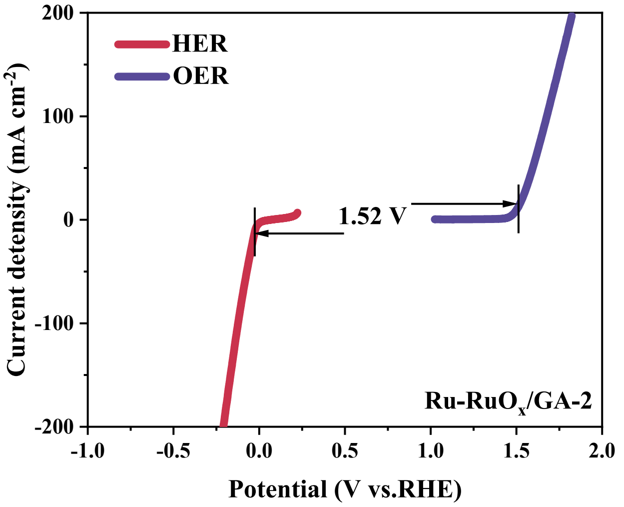

Figure S27. Theoretical electrolytic voltage to achieve a current density of 10 mA cm^{-2}.

Figure S28. (a) Optical photograph of the assembled electrolyzer. (b) Photographs of H_2 and O_2 collected at different times. (c) The amount of H_2 and O_2 varying with time.

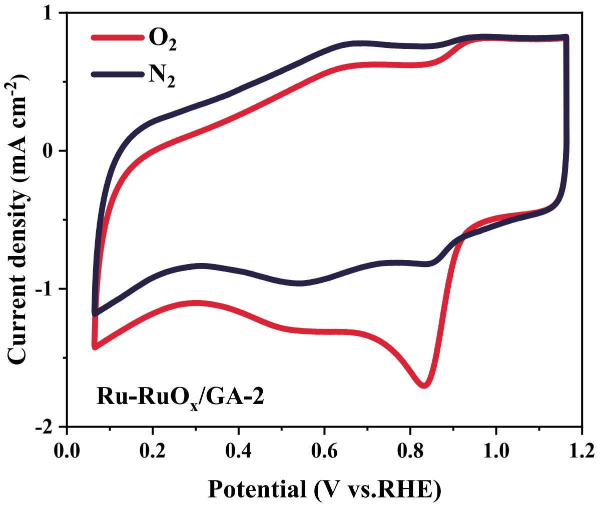

Figure S29. CV curves of Ru-RuO$_x$/GA-2 in both N$_2$-saturated and O$_2$-saturated 0.1 M KOH solution.

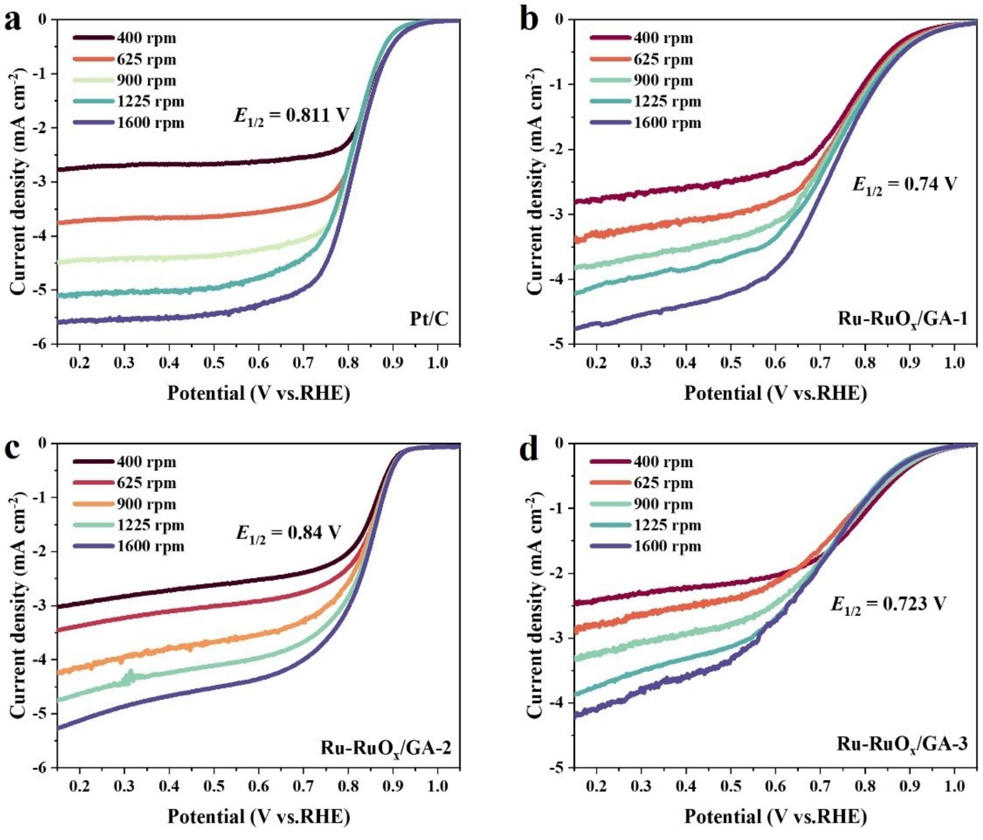

Figure S30. (a-d) ORR polarization curves in 0.1 M KOH with different rotating speed.

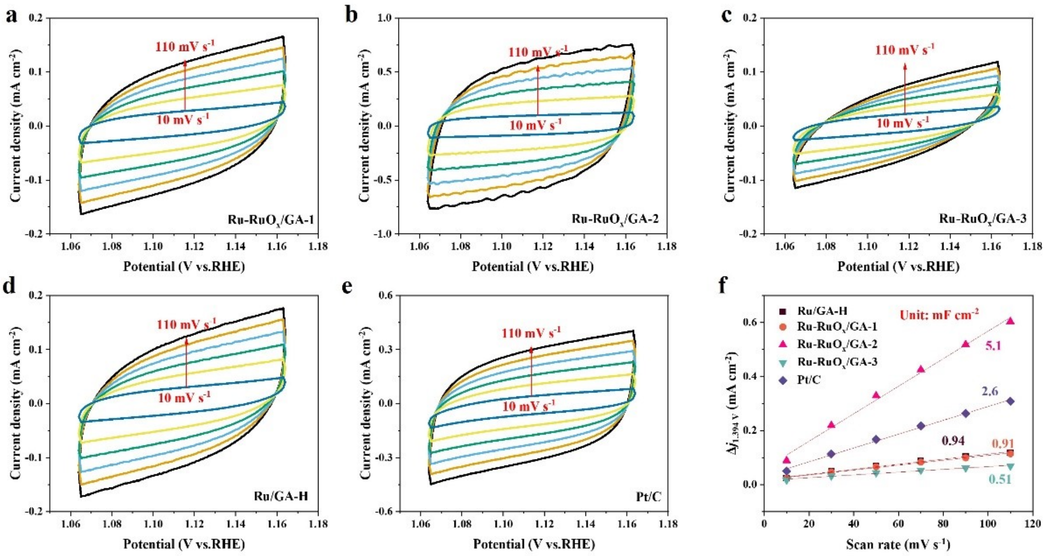

Figure S31. (a-e) CVs with different scan rates for Ru-RuO_x/GA-1, 2, 3, Ru/GA-H, and Pt/C. (f) C_{dl} values fitted according to CV curves.

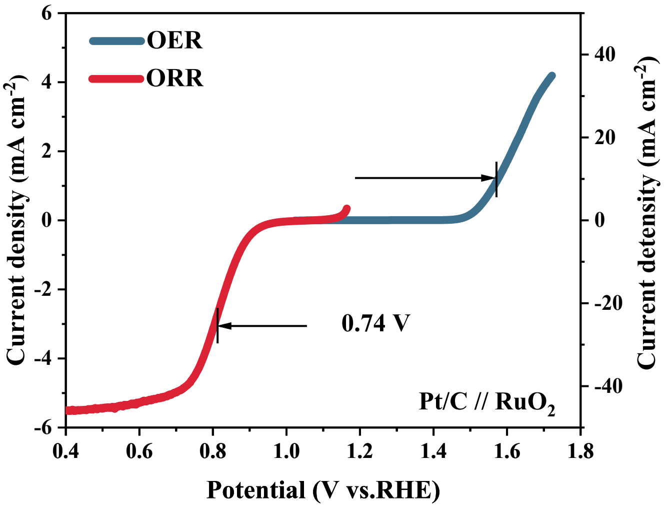

Figure S32. OER and ORR polarization curves of different electrocatalysts for Pt/C//RuO_2.

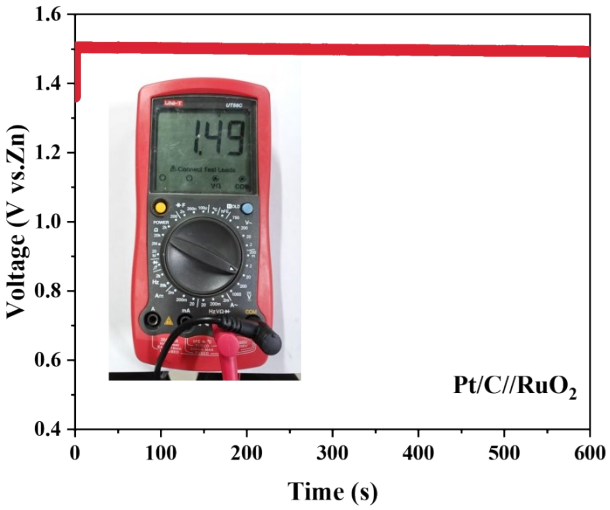

Figure S33. OCV profiles for Pt/C//RuO$_2$.

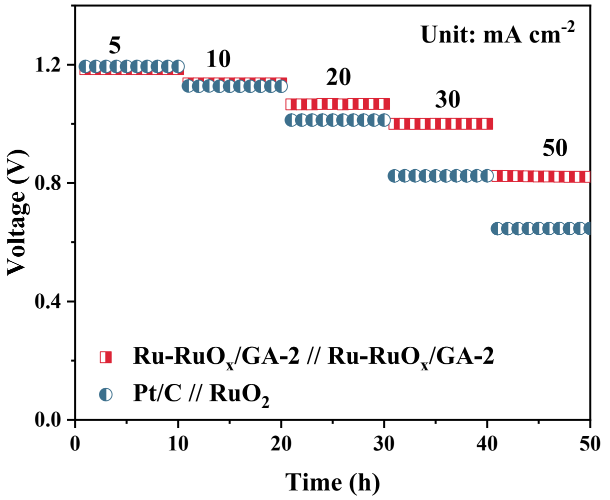

Figure S34. Galvanostatic discharge curves at various current densities of Ru-RuO$_x$/GA-2 and Pt/C//RuO$_2$ based ZABs.

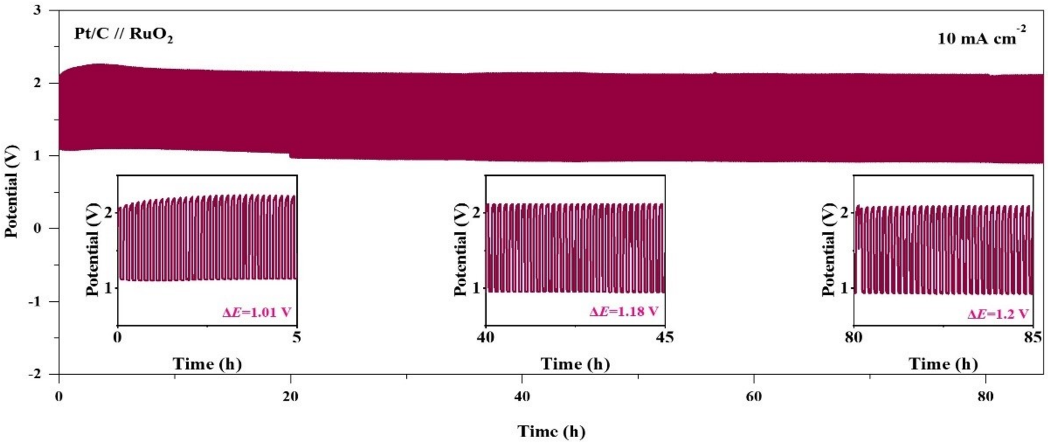

Figure S35. Long-term cycling stability of the ZABs at 10 mA cm^{-2}.

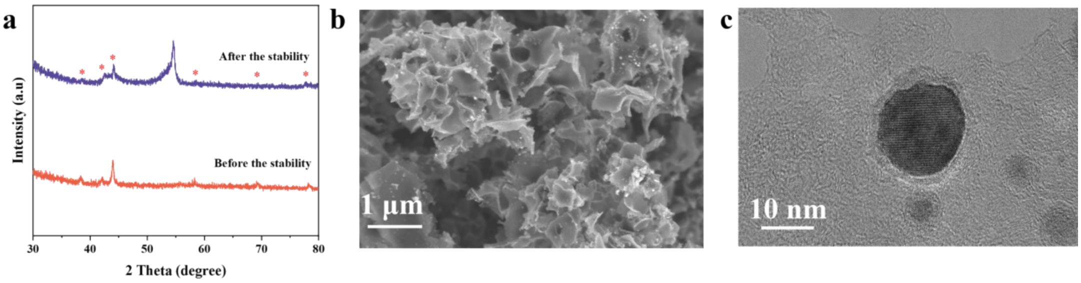

Figure S36. (a) XRD results before and after stability testing. (b-c) SEM and TEM results after stability testing.

Table S1. XPS results of Ru^{4+}/Ru^0 for different catalysts.

Catalysts	Ru^{4+}/Ru^0
Ru/GA-H	0
Ru-RuO_x/GA-1	0.62
Ru-RuO_x/GA-2	0.69
Ru-RuO_x/GA-3	0.80

Table S2. The EXAFS fitting results for different Ru samples.

Sample	path	CN	R/Å	σ^2/*10^3 Å	E_0	R-facter
Ru foil	Ru-Ru	1	2.67	0.00319	-8.73	0.011
Ru-RuO_x/GA-2	Ru-O	1.98	2.13	0.001	6.75	0.018
	Ru-Ru	2.08	2.83			
RuO_2	Ru-O	2	1.97	0.00292	1.90	0.012

CN is the coordination number; $S0^2$ for Ru is set as 0.829 recorded from literatures. R is interatomic distance (the bond length between central atoms and surrounding coordination atoms); σ^2 is Debye-Waller factor (a measure of thermal and static disorder in absorber-scatterer distances); E_0 is edge-energy shift (the difference between the zero kinetic energy value of the sample and that of the theoretical model).

Table S3. ECSA results of different Ru samples, Pt/C and RuO_2.

Catalysts	HER （cm^2）	OER （cm^2）	ORR （cm^2）
Ru/GA-H	175	217.5	23.5
Ru-RuO_x/GA-1	960	132.5	22.75
Ru-RuO_x/GA-2	2107.5	335	127.5
Ru-RuO_x/GA-3	247.5	145	13.25
Pt/C	585	--	65
RuO_2	--	165	--

Table S4. Comparison of HER performance of Ru-based catalysts.

Catalysts	Overpotential @10mA cm^{-2} (mV)	Stability	Multiple electro-catalysis	References
Ru-RuO_x/GA-2	17	200 h	HER/OER/ORR	**This work**
fcc Ru/C-NH_3	17	10000 cycles	HER/HOR	[14]
a/c-RuO_2/$Ni_{0.85}Se$	58	100 h	HER/OER	[15]
Ru/RuO_2-TiO_2	16.4	--	HER	[16]
Pd_2RuO_x	14	20 h	HER/OER/ORR	[17]
Co_1Ru@Ru/CN_x	30	10000st	HER	[18]
Ru@WNO-C	24	10000 cycles	HER	[19]
CeO_2-Ru	12.9	25 h	HER	[20]
Ru/Ni-N-C	20	48 h	HER	[21]
Ru/ac-ZrO_2	14	8000th	HER	[22]
Ru-ene	41	100 h	HER	[23]
RMNCL	19	100 h	HER/OER	[24]
RuP/Ru@CNS	15	24 h	HER	[25]
Ru/NC	21.9	1000 cycles	HER	[26]
Ru/WO_3-VO	21	40 h	HER	[27]

Table S5. Comparison of ZAB performance of different catalysts.

Catalysts	Open Voltage (V)	Discharge capacity (mAh g^{-1})	Stability	References
Ru-RuO_x/GA-2	1.56	946.4	300 h	**This work**
(NiFe-LDH)1/$GA_{0.18}$	1.50	725	220 h	[28]
CoFe-FeNC	1.447	767.5	1200 h	[29]
Mn_2O_3/RuO_2	1.45	742.1	850 h	[30]
Co-NCS-5‖Co_2P-NCS-60	1.50	--	60 h	[31]
$RuSe_2CoSe_2$/NC	1.52	--	140 h	[32]
C@Ir/CNF700	1.45	647.6	33 h	[33]
Pt@CoS_2-NrGO	1.41	763	55 h	[34]
MnO_2/Co_2P@SDHC	1.49	810.3	2800 h	[35]
Mo_2N-FeMo/HNCs	1.48	--	280 h	[36]
CoO-Mn_3O_4	1.43	802	100 h	[37]
Co-N-C@mHCSs	1.41	943.1	45 h	[38]
Co-FNC	1.55	817	300 h	[39]
Co@D-NCNT/CW	1.45	785.5	500 h	[40]
SA-Fe-SNC@900	1.464	798.7	200 h	[41]
CoN-BC-0.3	1.465	776.4	330 h	[42]

References

[1] G. Kresse, D. Joubert, From ultrasoft pseudopotentials to the projector augmented-wave method. *Physical review B*. **1999**, *59*, 1758.

[2] G. Kresse, J. Hafner, Ab initio molecular dynamics for liquid metals, *Physical review. B* **1993**, 47, 558-561.

[3] G. R. Su, S. Yang, S. Li, C. J. Butch, S. N. Filimonov, J. C. Ren, W. Liu, Switchable Schottky Contacts: Simultaneously Enhanced Output Current and Reduced Leakage Current, *J. Am. Chem. Soc.* **2019**, *141*, 1628-1635.

[4] S. Grimme, J. Antony, S. Ehrlich, H. Krieg, A consistent and accurate ab initio parametrization of density functional dispersion correction (DFT-D) for the 94 elements H-Pu, *J. Chem. Phys*. **2010**, 132.

[5] N. Shuichi, Constant Temperature Molecular Dynamics Methods. *Prog. Theor. Phys. Suppl*. **1991**, *103*, 1–46.

[6] H. J. Monkhorst, J. D. Pack, Special points for Brillouin-zone integrations. *Physical review B*. **1976**, *13*, 5188.

[7] Q. Li, Z. Sun, C. Yin, Y. Chen, D. Pan, B. Yu, Y. Zhang, T. He, S. Chen, Template-assisted synthesis of ultrathin graphene aerogels as bifunctional oxygen electrocatalysts for water splitting and alkaline/neutral zinc-air batteries, *Chem. Eng. J*. **2023**, *458*, 141492.

[8] H. Cui, Y. Guo, Z. Zhou, Three - Dimensional Graphene - Based Macrostructures for Electrocatalysis, *Small* **2021**, *17*, 2005255.

[9] X. Tang, Y. Wang, Z. Zhang, M. Xu, Z. Tao, S. Li, J. Liu, Z. Peng, C. Guo, L. He, R. Wang, M. Du, Z. Zhang, S. H. Kim, Flexible Zn-air battery for self-powered aptasensing SARS-CoV-2, *Nano Energy* **2024**, *127*, 109713.

[10] J. Wei, J. Lou, W. Hu, X. Song, H. Wang, Y. Yang, Y. Zhang, Z. Jiang, B. Mei, L. Wang, T. Yang, Q. Wang, X. Li, Superstructured Carbon with Enhanced Kinetics for Zinc - Air Battery and Self - Powered Overall Water Splitting, *Small* **2024**, *20*, 2308956.

[11] Y. Li, Y. Luo, Z. Zhang, Q. Yu, C. Li, Q. Zhang, Z. Zheng, H. Liu, B. Liu, S. Dou, Implanting Ru nanoclusters into N-doped graphene for efficient alkaline hydrogen evolution, *Carbon* **2021**, *183*, 362-367.

[12] L. Li, G. Zhang, C. Zhou, F. Lv, Y. Tan, Y. Han, H. Luo, D. Wang, Y. Liu, C. Shang, L. Zeng, Q. Huang, R. Zeng, N. Ye, M. Luo, S. Guo, Lanthanide-regulating Ru-O covalency optimizes acidic oxygen evolution electrocatalysis, *Nat. Commun*. **2024**, *15*, 4974.

[13] S. S. Xin, Y. Tang, B. H. Jia, Z. F. Zhang, C. P. Li, R. Bao, C. J. Li, J. H. Yi, J. S. Wang, T. Y. Ma, Coupling Adsorbed Evolution and Lattice Oxygen Mechanism in Fe-Co(OH)/FeO Heterostructure for Enhanced Electrochemical Water Oxidation, *Adv. Funct. Mater*. **2023**, *33*, 2305243.

[14] S. He, Y. Tu, J. Zhang, L. Zhang, J. Ke, L. Wang, L. Du, Z. Cui, H. Song, Ammonia-Induced FCC Ru Nanocrystals for Efficient Alkaline Hydrogen Electrocatalysis, *Small* **2024**, *20*, 2308053.

[15] L. Li, H. Sun, X. Xu, M. Humayun, X. Ao, M. F. Yuen, X. Xue, Y. Wu, Y. Yang, C. Wang, Engineering Amorphous/Crystalline Rod-like Core-Shell Electrocatalysts for Overall Water Splitting, *ACS Appl. Mater. Interfaces* **2022**, *14*, 50783–50793.

[16] Y. Yang, L. Xu, C. Li, R. Ning, J. Ma, M. Yao, S. Geng, F. Liu, Enhanced hydrogen evolution in neutral media via proximity effect of Ru/RuO_2-TiO_2 nanocatalysts, *J. Mater. Sci. Technol*. **2025**, *212*, 173-181.

[17] V.-H. Do, P. Prabhu, V. Jose, T. Yoshida, Y. Zhou, H. Miwa, T. Kaneko, T. Uruga, Y. Iwasawa, J.-M. Lee, Pd-PdO Nanodomains on Amorphous Ru Metallene Oxide for High-Performance Multifunctional Electrocatalysis, *Adv. Mater*. **2023**, *35*, 2208860.

[18] X. Bao, Y. Chen, S. Mao, Y. Wang, Y. Yang, Y. Gong, Boosting the Performance Gain of Ru/C for Hydrogen Evolution Reaction Via Surface Engineering, *Energy Environ. Mater*. **2023**, *6*, e12418.

[19] G. Meng, H. Tian, L. Peng, Z. Ma, Y. Chen, C. Chen, Z. Chang, X. Cui, J. Shi, Ru to W electron donation for boosted HER from acidic to alkaline on Ru/WNO sponges, *Nano Energy* **2021**, *80*, 105531.

[20] H. Fan, X. Wan, S. Sun, X. Zhou, X. Bu, J. Ye, R. Bai, H. Lou, Y. Chen, J. Gao, J. Zhang, W. Gao, D. Wen, Revealing the Role

of Ru-O-Ce Interface Coupling in CeO_2-Ru Aerogel for Boosting Hydrogen Evolution Kinetics, *Adv. Energy.Mater*. **2025**, *15*, 2405681.

[21] R. Yu, X. Cao, C. Zhu, Q. Chen, Z. Yan, B. Jiang, J. Mao, X. Wei, Asymmetric interfacial engineering regulated charge distribution on Ru/Ni-N-C sites for efficient hydrogen evolution reaction in alkaline and seawater electrolytes, *Sci China Chem*.**2025**, *68*, 3048–3055.

[22] J. Niu, H. Duan, T. Sun, Z. Zhi, D. Li, X. Fan, L. Zhang, D. Yang, Amorphous/Crystalline ZrO_2 with Oxygen Vacancies Anchored Nano-Ru Enhance Reverse Hydrogen Spillover in Alkaline Hydrogen Evolution, *Small* **2025**, 2410436.

[23] K. Deng, J. Yu, Q. Mao, R. Yang, H. Yu, Z. Wang, J. Wang, L. Wang, H. Wang, Superlattices in Ru Metallene Nanobelts for Robust Hydrogen Evolution, *Adv. Funct. Mater*. **2025**, *35*, 2420728.

[24] W. Ma, Y. Zhang, B. Wang, J. Wang, Y. Dai, L. Hu, X. Lv, J. Dang, Significantly enhanced OER and HER performance of NiCo-LDH and NiCoP under industrial water splitting conditions through Ru and Mn bimetallic co-doping strategy, *Chem. Eng. J*. **2024**, *494*, 153212.

[25] D. Li, R. Cai, D. Zheng, J. Ren, C.-L. Dong, Y.-C. Huang, S. J. Haigh, X. Liu, F. Gong, Y. Liu, J. Liu, D. Yang, A Sustainable Route to Ruthenium Phosphide (RuP)/Ru Heterostructures with Electron-Shuttling of Interfacial Ru for Efficient Hydrogen Evolution, *Adv. Sci*. **2024**, *11*, 2309869.

[26] S. Zhu, Z. Li, L. Hou, M. G. Kim, H. Jang, S. Liu, X. Liu, Revealing The Role of Electronic Asymmetricity on Supported Ru Nanoclusters for Alkaline Hydrogen Evolution Reaction, *Adv. Funct. Mater*. **2024**, *34*, 2314899.

[27] J. Cai, W. Zhang, Y. Liu, R. Shen, X. Xie, W. Tian, X. Zhang, J. Ding, Y. Liu, B. Li, Interfacial synergistic effect of Ru nanoparticles embedded onto amorphous/crystalline WO_3 nanorods on boosting the pH-universal hydrogen evolution reaction, *Appl. Catal., B*. **2024**, *343*, 123502.

[28] Q. Li, Z. Sun, C. Yin, Y. Chen, D. Pan, B. Yu, Y. Zhang, T. He, S. Chen, Template-assisted synthesis of ultrathin graphene aerogels as bifunctional oxygen electrocatalysts for water splitting and alkaline/neutral zinc-air batteries, *Chem. Eng. J*. **2023**, *458*, 141492.

[29] S. Zhang, J. Yang, L. Yang, T. Yang, Y. Liu, L. Zhou, Z. Xu, X. Zhou, J. Tang, Boosting ORR/OER bifunctional electrocatalysis by promoting electronic redistribution of Fe-N-C on CoFe-FeNC for ultra-long rechargeable Zn-air batteries, *Appl. Catal., B*. **2024**, *359*, 124485.

[30] X. Ma, M. Liu, Z. Xu, P. Qiao, Q. Li, R. Wang, S. Zhang, J. Zou, B. Jiang, Heterointerface engineering of yolk-shell-structured Mn_2O_3/RuO_2 for boosting oxygen electrocatalysis in rechargeable liquid and flexible zinc-air batteries, *Chem. Eng. J*. **2024**, *498*, 155118.

[31] J. Wei, J. Lou, W. Hu, X. Song, H. Wang, Y. Yang, Y. Zhang, Z. Jiang, B. Mei, L. Wang, T. Yang, Q. Wang, X. Li, Superstructured Carbon with Enhanced Kinetics for Zinc-Air Battery and Self-Powered Overall Water Splitting, *Small* **2024**, *20*, 2308956.

[32] L. Li, J. Qu, L. Zhang, L. Wei, J. Su, L. Guo, $RuSe_2$ and $CoSe_2$ Nanoparticles Incorporated Nitrogen-Doped Carbon as Efficient Trifunctional Electrocatalyst for Zinc-Air Batteries and Water Splitting, *ACS Appl. Mater. Interfaces* **2024**, *16*, 24660-24670.

[33] S.-W. Yoon, D.-K. Boo, H. Na, T.-Y. Kim, H.-S. Chang, J. S. Park, S.-H. Cho, J.-W. Jung, H. M. Jin, Facile encapsulation strategy for uniformly-dispersed catalytic nanoparticles/carbon nanofibers toward advanced Zn-air battery, *J. Mater. Chem. A*. **2025**, *13*, 3339-3349.

[34] N. Logeshwaran, S. Ramakrishnan, S. S. Chandrasekaran, M. Vinothkannan, A. R. Kim, S. Sengodan, D. B. Velusamy, P. Varadhan, J.-H. He, D. J. Yoo, An efficient and durable trifunctional electrocatalyst for zinc–air batteries driven overall water splitting, *Appl. Catal., B*. **2021**, *297*, 120405.

[35] W. Zhao, J. Chen, X. Liu, Y. Gao, J. Pu, Q. Cao, T. Meng, A. M. Elshahawy, S. A. Makhlouf, C. Guan, Prokaryote-Inspired and Derived Oxygen Reduction Electrocatalysts for Ultra-Long-Life Zn-Air Batteries, *Adv. Energy.Mater.* **2025**, *15*, 2405594.

[36] C.-Y. Wang, L. Zhang, J.-J. Feng, Y.-J. Gao, A.-J. Wang, Mo_2N nanoclusters and FeMo dual atomic active sites confined in N-doped hollow carbon nanocages for synergistic improvement in oxygen reduction and Zn-air battery, *Chem. Eng. J*. **2025**, *507*, 160442.

[37] J. H. Choi, H. Chun, D. W. Kim, M. K. Kabiraz, J. Kim, J. Kim, K.-H. Kim, B. Wang, H. M. Jeong, S.-I. Choi, B. Han, J. K. Kang, Zeolitic imidazolate framework-derived bifunctional CoO-Mn_3O_4 heterostructure cathode enhancing oxygen reduction/evolution via dynamic O-vacancy formation and healing for high-performance Zn-air batteries, *Energy Storage Mater.* **2025**, *75*, 104040.

[38] X. Tang, Y. Wang, Z. Zhang, M. Xu, Z. Tao, S. Li, J. Liu, Z. Peng, C. Guo, L. He, R. Wang, M. Du, Z. Zhang, S. H. Kim, Flexible Zn-air battery for self-powered aptasensing SARS-CoV-2, *Nano Energy* **2024**, *127*, 109713.

[39] D. Cao, Y. Mu, L. Liu, Z. Mou, S. Chen, W. Yan, H. Zhou, T.-S. Chan, L.-Y. Chang, L. Song, H.-J. Zhai, X. Fan, Axially Modified Square-Pyramidal CoN_4-F1 Sites Enabling High-Performance Zn-Air Batteries, *Acs Nano* **2024**, *18*, 11474-11486.

[40] Z. Chen, H. Chen, T. Li, X. Tian, K. Zhang, Y. Miao, C. Xia, L. Cai, B. Hui, C. Chen, Defective wood-based chainmail electrocatalysts boost performances of seawater-medium Zn-air batteries, *J. Energy Chem*. **2025**, *102*, 134-143.

[41] Z. Chen, X. Peng, Z. Chen, T. Li, R. Zou, G. Shi, Y. Huang, P. Cui, J. Yu, Y. Chen, X. Chi, K. P. Loh, Z. Liu, X. Li, L. Zhong, J. Lu, Mass Production of Sulfur-Tuned Single-Atom Catalysts for Zn-Air Batteries, *Adv. Mater*. **2023**, *35*, 2209948.

[42] Z. Chen, Y. Zou, H. Chen, K. Zhang, B. Hui, Bamboo-Modulated Helical Carbon Nanotubes for Rechargeable Zn-Air Battery, *Small* **2024**, *20*, 2307776.

Address correspondence to First A. Firstauthor, email1; Third C. Thirdauthor, email2